Journal of Industrial and Engineering Chemistry 75 (2019) 100–107

Contents lists available at ScienceDirect

Journal of Industrial and Engineering Chemistry

journal homepage: www.elsevier.com/locate/jiec

Multi-channel-contained few-layered $MoSe_2$ nanosheet/N-doped carbon hybrid nanofibers prepared using diethylenetriamine as anodes for high-performance sodium-ion batteries

Sun Young Jeong[a], Subrata Ghosh[b], Jae-Kwang Kim[c], Dong-Won Kang[d], Sang Mun Jeong[b,*], Yun Chan Kang[e,*], Jung Sang Cho[a,*]

[a] Department of Engineering Chemistry, Chungbuk National University, Chungbuk 361-763, Republic of Korea
[b] Department of Chemical Engineering, Chungbuk National University, Chungbuk 361-763, Republic of Korea
[c] Department of Solar & Energy Engineering, Cheongju University, Cheongju, Chungbuk, 28503, Republic of Korea
[d] School of Energy Systems Engineering, Chung-Ang University, Seoul 06974, Republic of Korea
[e] Department of Materials Science and Engineering, Korea University, Anam-Dong, Seongbuk-Gu, Seoul 136-713, Republic of Korea

ARTICLE INFO

Article history:
Received 12 November 2018
Received in revised form 21 February 2019
Accepted 5 March 2019
Available online 15 March 2019

Keywords:
Molybdenum diselenide
Sodium ion batteries
Anodes
Multi-channel
Nanofibers
Electrospinning

ABSTRACT

A facile new strategy for the synthesis of multi-channel-contained N-doped carbon nanofibers composed of few-layered $MoSe_2$ nanosheets (denoted as MC-NCNF/$MoSe_2$) was introduced and the composite was demonstrated as an anode material for sodium-ion batteries. This was the first time that diethylenetriamine was introduced as a pore generator in the electrospinning process and played a key role in generating multi-channels in the structure by phase-separation from the molybdenum salt and subsequent volatilization without any additional process. Polyvinylpyrrolidone was used as a carbon precursor and played the role of a N-doping source for the carbon matrix. MC-NCNF/$MoSe_2$ achieved a high reversible discharge capacity of 386 mA h g^{-1} at a current density of 0.5 A g^{-1} after the 300th cycle and superior rate capability of 285 mA h g^{-1} at 10.0 A g^{-1}. The multi-channeled structure of MC-NCNF/$MoSe_2$ facilitated effective Na^+ and electron diffusion during repeated discharge/charge processes and accommodated the huge volume expansion of the $MoSe_2$ nanosheets induced by electrochemical reaction of the Na^+ ion.

Introduction

Recently, sodium-ion batteries (SIBs) have been considered as next-generation energy storage devices due to the abundance of Na resources and the electrochemical similarity of Na to Li [1–5]. Despite significant advances in SIBs, many challenges must be addressed for practical application. The major obstacle in the design of anode materials for SIBs is the slow Na^+ diffusion rate and large volume expansion induced by the large ionic radius and molecular weight of Na^+, which result in low capacity, short cycle life-time, and poor rate performance. Therefore, many approaches have been proposed toward engineering anode materials with suitable geometries and compositions to solve the above-mentioned problems [6–9]. Hollow and porous 1-dimensional (1-D) nanomaterials have received widespread attention because they shorten the pathway for Na^+ diffusion into the structure, lower the strain of the active material under volume variation, and allow penetration of the liquid electrolyte into the electrode during cycling [10–13]. Wu et al. introduced porous TiO_{2-x} nanofibers rich in oxygen vacancies and possessing high grain-boundary densities by employing electrospinning and subsequent vacuum treatment [10]. The oxygen vacancies in the composites improved the electronic conductivity and promoted fast Na^+ diffusion. Therefore, the TiO_{2-x} nanofibers showed excellent long cycling stability (134 mA h g^{-1} at 10 C after 4500 cycles) and superior rate performance (93 mA h g^{-1} after 4500 cycles at 20 C). Liu et al. also synthesized Sn nanodots (1–2 nm) encapsulated in porous N-doped carbon nanofibers by electrospinning and thermal treatment methods [11]. The small Sn nanodots could reduce the strain and improve the rate of utilization of the active materials during the sodiation/desodiation process. Therefore, capacities of 450 mA h g^{-1} at 10,000 mA g^{-1} and 483 mA h g^{-1} at 2000 mA g^{-1} were achieved over 1300 cycles. Li et al. also proposed porous carbon

* Corresponding authors.
E-mail addresses: smjeong@cbnu.ac.kr (S. Mun Jeong), yckang@korea.ac.kr (Y. Chan Kang), jscho@cbnu.ac.kr (J.S. Cho).

https://doi.org/10.1016/j.jiec.2019.03.007
1226-086X/

nanofibers prepared by pyrolysis of PAN-F127/DMF nanofibers via an electrospinning process [12]. The triblock copolymer Pluronic F127 was used as a pore generator during heat-treatment. The nanofibers delivered a reversible capacity of 266 mA h g^{-1} after 100 cycles at 0.2 C. A reversible capacity of 140 mA h g^{-1} was still delivered after 1000 cycles at a current density of 500 mA g^{-1}.

Layered transition metal chalcogenides have recently attracted great attention for SIB anodes due to their superior energy storage properties compared to those of other oxides [14–17]. In particular, $MoSe_2$, consisting of covalently bonded Se-Mo-Se sandwiched layers with weak van der Waals interactions, possesses a relatively large interlayer spacing of 0.65 nm compared to graphite (0.335 nm) and MoS_2 (0.615 nm), and higher electrical conductivity compared to MoS_2. Therefore, such unique features of $MoSe_2$ anodes facilitate faster and reversible sodiation/desodiation of Na^+ ion between the layers [18–21].

Hence, we introduce a facile new strategy for the synthesis of multi-channel-contained N-doped carbon nanofibers composed of few-layered $MoSe_2$ nanosheets as promising anode materials for SIBs for the first time. Diethylenetriamine (DETA) is introduced as a pore generator for the first time in this study. DETA plays a key role in generating the mesoporous multi-channels in the structure by phase-separation from the molybdenum salt during the electrospinning process and subsequent volatilization during stabilization at low temperature. Additionally, polyvinylpyrrolidone (PVP) is used as a carbon precursor and plays the role of a N-doping source for the carbon matrix. The mechanism of formation of the multi-channel-contained N-doped carbon nanofibers composed of few-layered $MoSe_2$ nanosheets and the Na^+ ion storage properties of this material as an anode are investigated in detail.

Experimental

The multi-channel-contained N-doped carbon nanofibers composed of few-layered $MoSe_2$ nanosheets (denoted as MC-NCNF/$MoSe_2$) were synthesized via electrospinning and

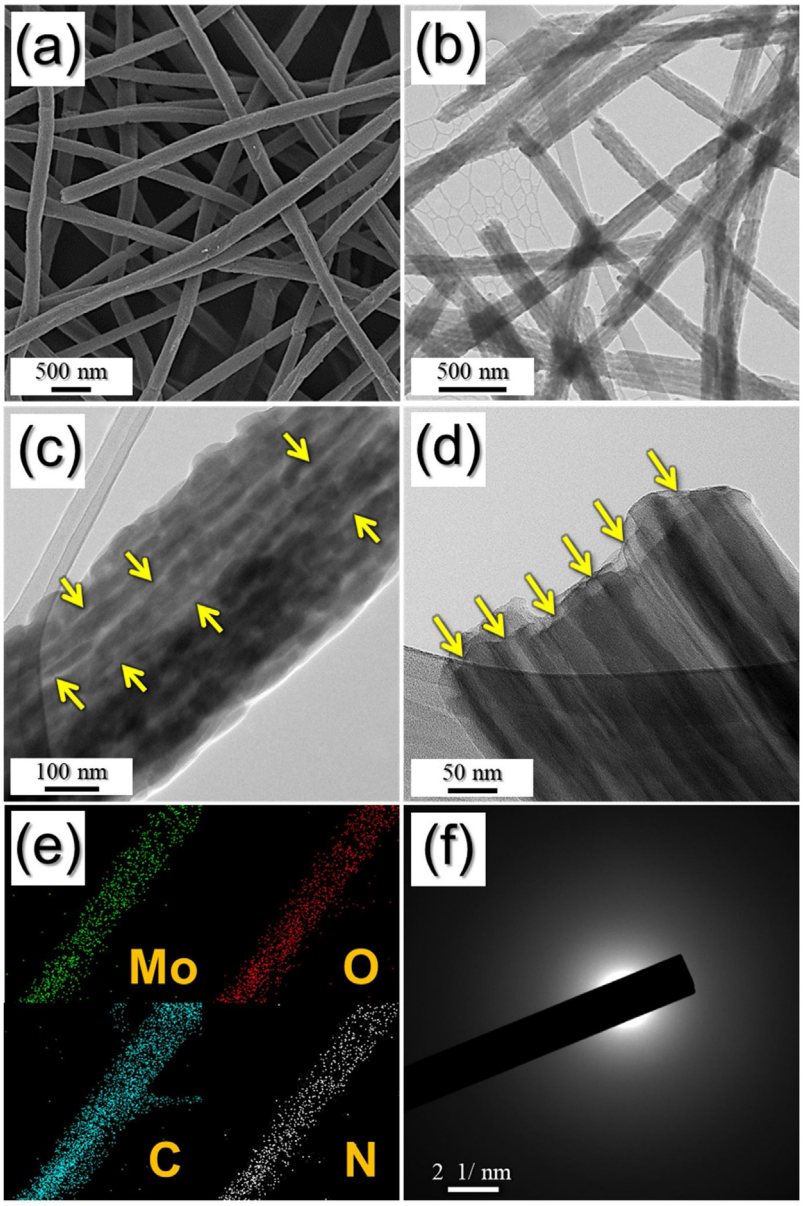

Fig. 1. Morphologies, SAED pattern, and elemental mapping images of the as-spun nanofiber after stabilization at 150 °C in air: (a) FE-SEM image, (b) TEM image, (c) and (d) HR-TEM images, (e) elemental mapping images, and (f) SAED pattern.

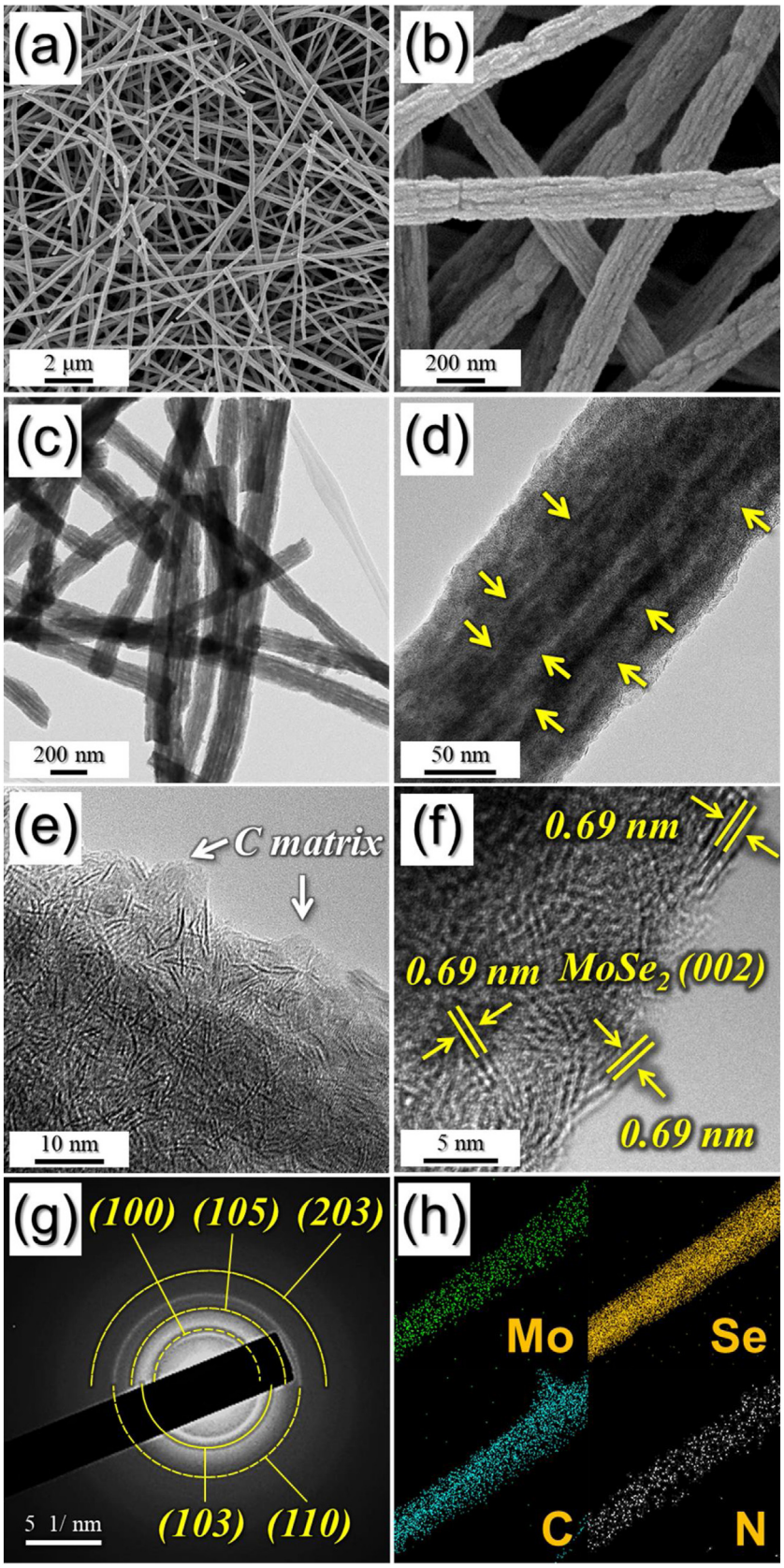

Fig. 2. Morphologies, SAED pattern, and elemental mapping images of MC-NCNF/$MoSe_2$: (a) and (b) FE-SEM images, (c) TEM image, (d) and (e) HR-TEM images, (f) HR lattice image, (g) SAED pattern, and (h) elemental mapping images.

subsequent simple heat-treatment. The solution for electrospinning was prepared by dissolving 1.3 g ammonium molybdate ($(NH_4)_6Mo_7O_{24}\,4H_2O$, DAEJUNG, 98%), 1.0 g polyvinylpyrrolidone (PVP, $(C_6H_9NO)_n$, Alfa Aesar, MW: 1300,000), and 1 mL diethylenetriamine (DETA, $C_4H_{13}N_3$, JUNSEI, 98%) in 10 mL of distilled water. The solution for electrospinning was transferred into a plastic syringe equipped with a 25-gauge stainless steel nozzle and ejected at a flow rate of 0.5 mL h^{-1} onto a drum collector covered with aluminum foil. The distance between the nozzle tip and drum collector was maintained at 12 cm and the rotation rate of the drum collector was 180 rpm. The applied voltage between the nozzle tip and drum collector was 20 kV. The as-spun nanofibers were stabilized at 150 °C for 1 day under ambient conditions. Heat-treatment was carried out at 400 °C for 10 h under a 5% H_2/Ar atmosphere with selenium metal powder (Se, SAMCHUN, 99.5%). During heat-treatment, H_2Se gas was formed by the reaction of H_2 with Se metal powder. The detailed information of the characterization techniques and electrochemical measurements of the samples are described in the supporting information and our previous article [22].

Results and discussion

The multi-channel-contained N-doped carbon nanofibers composed of few-layered $MoSe_2$ nanosheets (denoted as MC-NCNF/$MoSe_2$) were synthesized by electrospinning and subsequent heat-treatment. For this purpose, precursor Mo salt/PVP/DETA composite nanofibers were firstly prepared by electrospinning the aqueous solution with ammonium molybdate, PVP as the carbon precursor, and DETA as a pore generator. The as-spun nanofibers, stabilized at 150 °C under air atmosphere, are shown in Fig. 1. As is clear from Fig. 1a, uniform smooth-surfaced nanofibers with an average diameter of 380 nm were observed. The TEM and HR-TEM images (Fig. 1b–d) show obvious longitudinal multi-channels with a width of 10–20 nm along the fiber length direction. The DETA added to the aqueous solution was phase-separated from the Mo-salt because of low compatibility, as confirmed by the digital image in Fig. S1a (in Supplementary material), in which the mixed suspension did not become clear overnight. However, phase-separation between PVP and DETA did not occur in the system presented in Fig. S1b (in Supplementary material). Therefore, DETA was phase-separated from the Mo salt/PVP solution during electrospinning and evaporated from the as-spun nanofibers during stabilization at 150 °C overnight due to its high volatility, thus generating mesoporous longitudinal multi-channels in the nanofiber structure. The elemental mapping images in Fig. 1e show that Mo, O, N, and C were homogeneously distributed in the nanofiber structure. Although the SAED pattern (Fig. 1f) showed an amorphous-like ring-pattern, a poorly crystalline $(NH_4)Mo_3O_{10}\,H_2O$ phase was confirmed from the XRD data in Fig. S2. Therefore, the nanofibers after stabilization are assumed to be composed of $(NH_4)Mo_3O_{10}\,H_2O$ and PVP.

In order to perform both selenization and carbonization of the as-spun nanofibers, the nanofibers were post heat-treated at 400 °C under H_2/Ar atmosphere with Se powder in a covered alumina boat. Complete conversion of the Mo-salt in the nanofibers into the hexagonal $MoSe_2$ phase with low crystallinity was confirmed from the XRD data in Fig. S3. Therefore, the nanofibers obtained after heat-treatment were composed of $MoSe_2$ and carbon from the decomposed PVP. The detailed morphologies of the composite nanofibers after heat-treatment are shown in Fig. 2. The overall nanofiber morphology was well preserved even after heat-treatment, as shown in Fig. 2a–c. Moreover, the longitudinal multi-channels in the structure along the fiber length direction (indicated by the arrows) were also well preserved even after heat-treatment (Fig. 2d). However, single or two layered-$MoSe_2$ nanosheets with a mean width of 5 nm were newly formed in the carbon matrix, as shown in the HR-TEM image in Fig. 2e. The few-layered $MoSe_2$ nanosheets were uniformly distributed in the carbon matrix, as indicated by the arrows in Fig. 2e. Crystal growth and stacking of the $MoSe_2$ nanosheets were efficiently prevented by the surrounding carbon material [18,23,24]. Therefore, the few-layered $MoSe_2$ nanosheets formed in the carbon matrix are expected to improve the ionic/electronic conductivity by increasing the contact area between the electrolyte and $MoSe_2$ nanosheets during cycling [19,23,24]. The HR-TEM image in Fig. 2f shows clear lattice fringes separated by 0.69 nm, corresponding to the (002) plane of $MoSe_2$, which is slightly wider than that of natural $MoSe_2$ (0.65 nm) due to deintercalation of the intercalated NH_4^+ between the $MoSe_2$ lattices during selenization [25,26]. The expanded lattice spacing between the $MoSe_2$ layers is expected to enhance the kinetics of Na^+ intercalation-deintercalation during cycling, thus improving the rate capability and reversible capacity for Na^+ storage. The selected area electron diffraction (SAED) pattern in Fig. 2g shows the ill-defined ring pattern, which reveals that stacking of the $MoSe_2$ nanosheets was effectively prevented in the carbon matrix, which is consistent with the XRD data (Fig. S3 in Supplementary material). The elemental mapping images in Fig. 2h confirm the uniform distribution of the few-layered $MoSe_2$ nanosheets in the carbon matrix. Furthermore, well-distributed N was also detected, which suggests that N-doping into the carbon matrix occurred during heat-treatment. The N-doped carbon is expected to furnish improved electrical conductivity and electrochemical reactivity of the multi-channel-contained $MoSe_2$ composite nanofibers. Additionally, the defects formed in the N-doped carbon matrix could provide additional Na^+ insertion sites, which

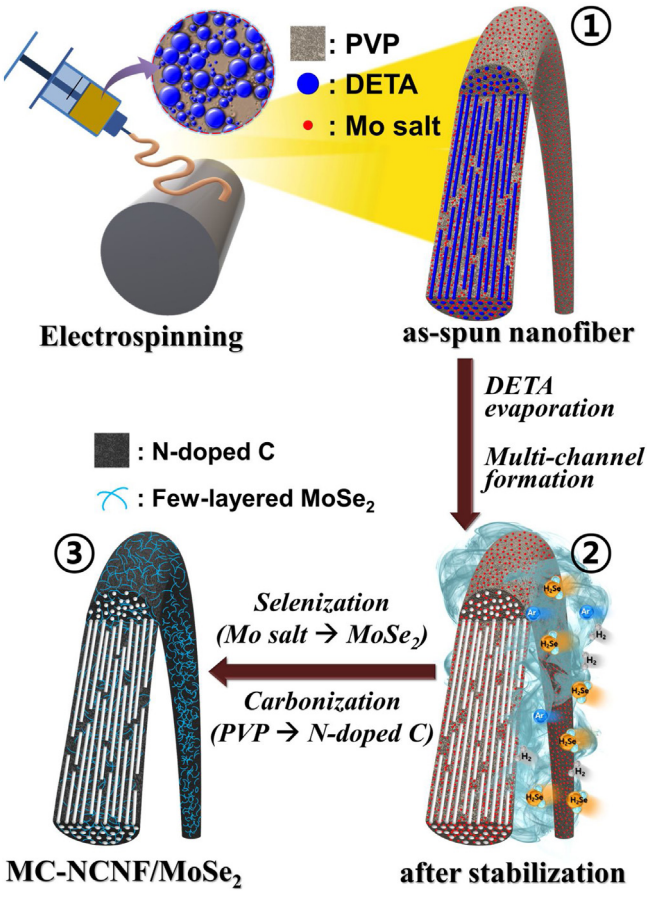

Scheme 1. Detailed formation mechanism of the multi-channel contained N-doped carbon nanofibers composed of few-layered $MoSe_2$ nanosheets.

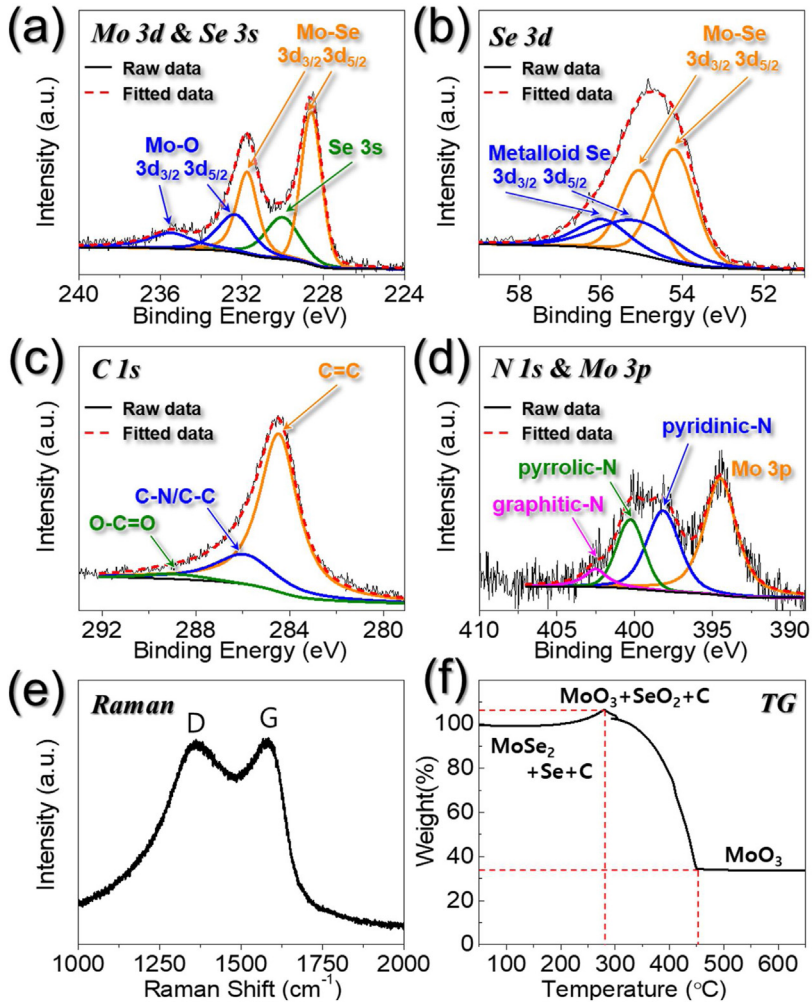

Fig. 3. XPS spectra, Raman spectrum, and the TG curve of MC-NCNF/$MoSe_2$: (a) Mo 3d XPS spectrum, (b) Se 3d XPS spectrum, (c) C 1s XPS spectrum, (d) N 1s XPS spectrum, (e) Raman spectrum, and (f) TG curve.

should enhance the Na^+ storage ability [27,28]. From the above results, the formation mechanism of MC-NCNF/$MoSe_2$ is briefly illustrated in Scheme 1.

To probe the bonding environment of the elements, XPS evaluation of MC-NCNF/$MoSe_2$ was carried out, as shown in Fig. 3a–d. All high-resolution XPS profiles were deconvoluted after subtracting the Shirley background. In the Mo 3d and Se 3 s region (Fig. 3a), two strong peaks with binding energies of 231.7 and 228.6 eV were observed, which correspond to the Mo $3d_{3/2}$ and Mo $3d_{5/2}$ states of Mo in the $MoSe_2$ nanosheets, respectively [20,29]. Mo-Se bonding was also observed based on the Se 3d spectrum (Fig. 3b), where the peaks at 55.0 and 54.2 eV correspond to the Se $3d_{3/2}$ and Se $3d_{5/2}$ states of Se in the $MoSe_2$ nanosheets, respectively [20,29]. The minor peaks related to Mo-O bonding at 235.5 and 232.3 eV are attributed to the partial surface oxidation of the sample under air [18,29,30]. A Se 3 s peak at 230.0 eV (Fig. 3a) and Se 3d peaks at 56.0 and 55.3 eV (Fig. 3b) were also detected in the structure, which are attributed to intercalation of the metalloid Se into the N-doped carbon matrix to some degree during selenization [31,32]. However, the amount of intercalated Se was assumed to be low because no corresponding peak was observed in the XRD spectrum (Fig. S3). The C 1s spectrum (Fig. 3c) showed several peaks related to C=C, C—N/C—C, and O—C=O bonds at 284.4, 286.0, and 288.9 eV, respectively [33–35]. N-doping into carbon was confirmed from the N 1s spectrum (Fig. 3d). The N 1s spectrum showed graphitic-N, pyrrolic-N, and pyridinic-N at binding energies of 402.5, 400.2, and 398.1 eV, respectively, along with a Mo 3p signal at 394.5 eV [36–40]. The graphitic- and pyridinic-N were bonded to two sp^2 C atoms at the edge of the carbon plane and to three C atoms within the graphene plane, respectively [41]. The pyrrolic N was assigned to N atoms in a five-membered heterocyclic ring. The Raman spectrum of MC-NCNF/$MoSe_2$ (Fig. 3e) showed D (1361 cm^{-1}) and G (1584 cm^{-1}) bands, indicating the structural disorder of carbon [42,43]. The relative intensity ratio of the D to G band (I_D/I_G) of MC-NCNF/$MoSe_2$ was 1.1, which proved the existence of structural defects, including bonding disorders generated by amorphous carbon. The TGA curve of MC-NCNF/$MoSe_2$ under air atmosphere is shown in Fig. 3f. The TG curve includes a one-step weight increase and subsequent one-step weight loss. The weight increase below 270 °C is attributed to decomposition of the $MoSe_2$ nanosheets into MoO_3 and SeO_2 [18,21]. Thereafter, both vaporization of SeO_2 and combustion of N-doped carbon resulted in the final residue of MoO_3, which induced a weight loss up to 450 °C The C and N contents in MC-NCNF/$MoSe_2$ were approximately 16 and 3 wt%, respectively, from the elemental analysis in Table S1 (in Supplementary material). Fig. S4 (in Supplementary material) shows the N_2 adsorption and desorption isotherms and Barrett-Joyner-Halenda pore distribution curves of MC-NCNF/$MoSe_2$. The isotherms of MC-NCNF/$MoSe_2$ shown in Fig. S4a were type IV with H4 hysteresis loops, indicating the presence of mesoporous multi-channels in the structure. The wide distribution of mesopores

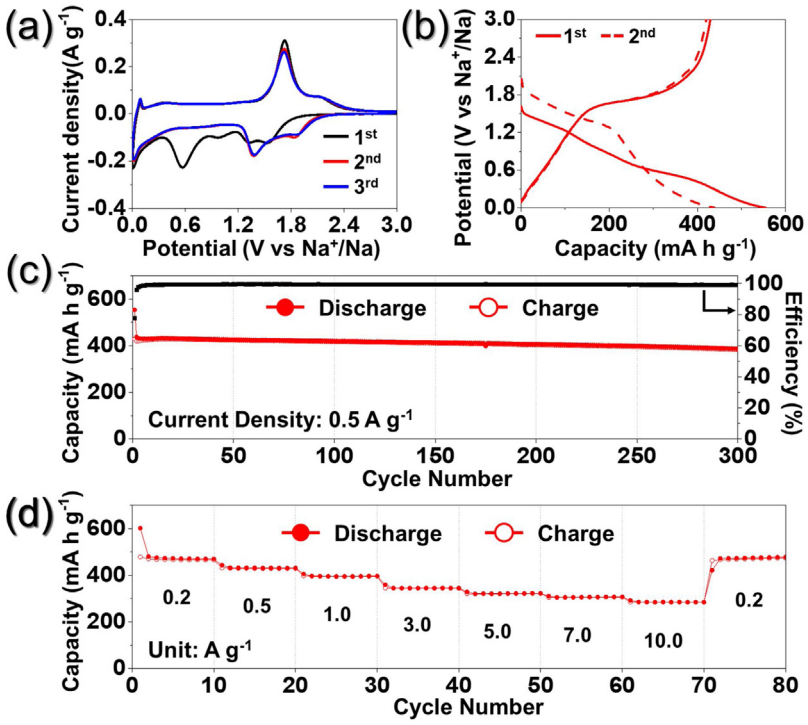

Fig. 4. Electrochemical properties of MC-NCNF/$MoSe_2$: (a) CV curves, (b) discharge–charge curves at a current density of 0.5 A g^{-1}, (c) cycling performance at 0.5 A g^{-1} and Coulombic efficiencies, and (d) rate performance.

between 3 and 50 nm is attributed to the multi-channels and the very sharp peak at 3.8 nm is due to the tensile strength effect based on the pore distribution curve in Fig. S4b [44].

To validate the potential as SIB anode materials, the electrochemical performance of MC-NCNF/$MoSe_2$ was evaluated, as shown in Fig. 4. Cyclic voltammetry (CV) of MC-NCNF/$MoSe_2$ was performed for the first three cycles at 0.1 mV s^{-1} over the potential range of 0.001–3.0 V (Fig. 4a). In the first cathodic scan, five peaks were detected, where the two peaks located at 1.53 and 1.33 V are ascribed to the electrochemical reaction of Na^+ with the residual metalloid Se intercalated in the N-doped carbon matrix during selenization and formation of Na_xMoSe_2 by intercalation of Na^+ into $MoSe_2$, respectively [18,19,45]. In addition, the peaks at 0.98 and 0.57 V are attributed to formation of the solid electrolyte interface (SEI) layer and conversion of Na_xMoSe_2 into $NaSe_2$ with Mo [18,19,46]. The final cathodic peak at 0.01 V is attributed to Na^+ intercalation into N-doped carbon [27,35,47,48]. The new peaks at 1.84 and 1.38 V that appeared after the second cycle are attributed to Na^+ insertion into $MoSe_2$ [18,19]. In the anodic scan, the first peak at 0.09 V is attributed to the deintercalation of Na^+ from the N-doped carbon matrix [28,36,47,48]. Additionally, the sharp peak at 1.73 V and accompanying shoulder peak at 2.12 V are assigned to the conversion of $NaSe_2$ with Mo into $MoSe_2$ with Na^+ [18,19]. From the third scan, the CV curves overlapped well, indicating the good stability and reversibility of MC-NCNF/$MoSe_2$ during the repeated sodiation/desodiation process. The two initial discharge-charge profiles of MC-NCNF/$MoSe_2$ at the current density of 0.5 A g^{-1} are shown in Fig. 4b. The profiles were consistent with the CV curves. The initial discharge capacity and Coulombic efficiency of MC-NCNF/$MoSe_2$ were 553 mA h g^{-1} and 77.3%, respectively. The initial irreversible capacity loss was accompanied by SEI layer formation derived from electrolyte decomposition and the carbonaceous material [49–52].

The cycling performance of MC-NCNF/$MoSe_2$ at a current density of 0.5 A g^{-1} is shown in Fig. 4c. MC-NCNF/$MoSe_2$ exhibited a discharge capacity of 386 mA h g^{-1} and 98.7% Coulombic efficiency after 300 cycles and stable cycle ability during cycling.

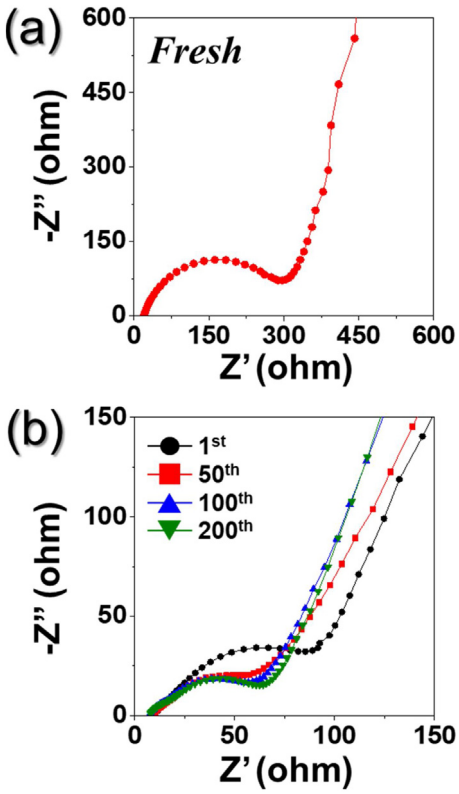

Fig. 5. Nyquist impedance plots of MC-NCNF/$MoSe_2$: (a) before cycling and (b) after cycling.

The numerous mesoporous multi-channels in the structure and N-doped carbon matrix facilitated accommodation of the huge volume expansion of the $MoSe_2$ nanosheets during repeated cycling. The rate performance of MC-NCNF/$MoSe_2$ is shown in

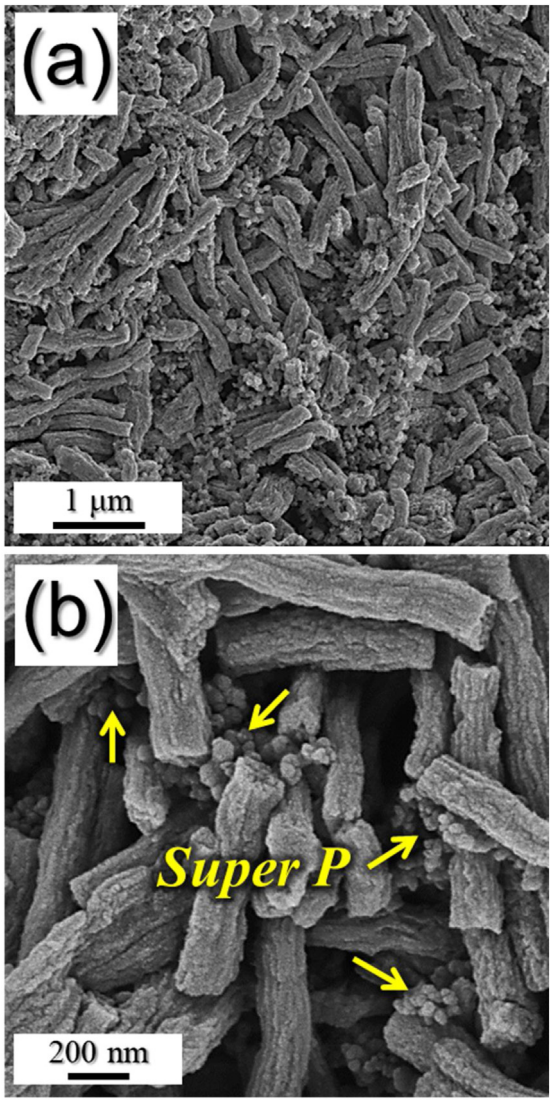

Fig. 6. Morphologies of MC-NCNF/$MoSe_2$ after 100 cycles at 0.5 A g^{-1}: (a) low- and (b) high-magnification FE-SEM images.

Fig. 4d, where the current density increased stepwise from 0.2 to 10.0 A g^{-1}, and then decreased to 0.2 A g^{-1}. The electrode delivered final discharge capacities of 470, 431, 397, 345, 322, 307, and 285 mA h g^{-1} at current densities of 0.2, 0.5, 1.0, 3.0, 5.0, 7.0, and 10.0 A g^{-1}, respectively. Furthermore, the discharge capacity recovered well to 478 mA h g^{-1} when the current density was decreased to 0.2 A g^{-1}, indicating superior reversibility of MC-NCNF/$MoSe_2$. The high electrical conductivity induced by the few-layered $MoSe_2$ nanosheets and N-doped carbon, the facile penetration of the liquid electrolyte into the electrode through the mesoporous multi-channels and shortening of the path for Na^+ diffusion between the electrode and electrolyte resulted in superior rate performance of MC-NCNF/$MoSe_2$. The electrochemical performance of MC-NCNF/$MoSe_2$ was compared with those of other reported $MoSe_2$ nanostructures with various morphologies, as summarized in Table S2 (in Supplementary material). MC-NCNF/$MoSe_2$ prepared in this study showed superior electrochemical properties for Na^+ storage even at high current density.

To gain insight into the electrochemical performance of MC-NCNF/$MoSe_2$, electrochemical impedance spectroscopy (EIS) data were acquired (Fig. 5). EIS measurements were carried out on the electrodes before and after 1, 50, 100, and 200 cycles over the frequency range of 0.01 Hz to 100 kHz. The semicircles in the medium-frequency range of the Nyquist plots could be used to deduce the charge-transfer resistance (R_{ct}) of the electrode [53–56]. The R_{ct} value of MC-NCNF/$MoSe_2$ before cycling was 321 Ω. After the first cycle, the R_{ct} declined to approximately 90 Ω and was similar at 61 Ω after 50, 100, and 200 cycles. This result demonstrates the excellent stability of MC-NCNF/$MoSe_2$ for repeated Na^+ insertion and deinsertion over 200 cycles. To evaluate the structural stability, the morphology of MC-NCNF/$MoSe_2$ after 100 cycles was inspected, as shown in Fig. 6. Impressively, the MC-NCNF/$MoSe_2$ exhibited a robust structure that did not undergo pulverization, which ensured good tolerance of MC-NCNF/$MoSe_2$ against the huge volume expansion during repeated Na^+ insertion and deinsertion. The promising electrochemical behavior and robust nature of MC-NCNF/$MoSe_2$ are attributed to the excellent capacity to accommodate volume expansion due to the available mesoporous multi-channels in the structure, short Na^+ diffusion path between the electrode and electrolyte, and excellent electron transport via N-doped carbon.

Conclusions

We introduced a facile new strategy for the synthesis of multi-channel-contained N-doped carbon nanofibers composed of few-layered $MoSe_2$ by electrospinning and subsequent simple heat-treatment methods. A mechanism for the formation of MC-NCNF/$MoSe_2$ was proposed and the potential of this composite as an anode for Na^+ storage was demonstrated. Mesoporous multi-channels were formed along the fiber length direction by phase-separation between DETA and the molybdenum salt/PVP solution. During heat-treatment, the N in PVP acted as a N-doping source for the carbon matrix. With the beneficial features of the few-layer $MoSe_2$ nanosheets, mesoporous multi-channels, and the presence of N-doped carbon in the structure, MC-NCNF/$MoSe_2$ delivered a superior discharge capacity of 386 mA h g^{-1} even at a high current density of 0.5 A g^{-1} after 300 cycles when used as a SIB anode material. The simple strategy for synthesis of the multi-channel-contained transition metal chalcogenide composite nanofiber with N-doped carbon introduced in this study is expected to offer practical feasibility for developing promising anodes for SIBs, and the developed materials may find uses in a wide range of applications.

Acknowledgements

This work was supported by the National Research Foundation of Korea (NRF) grant funded by the Korea government (MSIP) (NRF-2018R1A4A1024691, NRF-2017M1A2A2087577, NRF-2018R1D1A3B07042514).

Appendix A. Supplementary data

Supplementary material related to this article can be found, in the online version, at doi:https://doi.org/10.1016/j.jiec.2019.03.007.

References

[1] B. Sun, P. Li, J. Zhang, D. Wang, P. Munroe, C. Wang, P.H. Notten, G. Wang, Adv. Mater. 30 (2018) 1801334.
[2] S.W. Kim, D.H. Seo, X. Ma, G. Ceder, K. Kang, Adv. Energy Mater. 2 (2012) 710.
[3] J. Sun, H.-W. Lee, M. Pasta, H. Yuan, G. Zheng, Y. Sun, Y. Li, Y. Cui, Nat. Nanotechnol. 10 (2015) 980.
[4] M.D. Slater, D. Kim, E. Lee, C.S. Johnson, Adv. Funct. Mater. 23 (2013) 947.
[5] Z. Li, J. Ding, D. Mitlin, Acc. Chem. Res. 48 (2015) 1657.
[6] L. Zhao, J. Zhao, Y.S. Hu, H. Li, Z. Zhou, M. Armand, L. Chen, Adv. Energy Mater. 2 (2012) 962.
[7] Y. Zhu, X. Han, Y. Xu, Y. Liu, S. Zheng, K. Xu, L. Hu, C. Wang, ACS Nano 7 (2013) 6378.

[8] S. Yuan, X. Huang, D. Ma, H. Wang, F. Meng, X. Zhang, Adv. Mater. 26 (2014) 2273.
[9] J.S. Cho, S.Y. Lee, J.-K. Lee, Y.C. Kang, ACS Appl. Mater. Interfaces 8 (2016) 21343.
[10] Y. Wu, Y. Jiang, J. Shi, L. Gu, Y. Yu, Small 13 (2017) 1700129.
[11] Y. Liu, N. Zhang, L. Jiao, J. Chen, Adv. Mater. 27 (2015) 6702.
[12] W. Li, L. Zeng, Z. Yang, L. Gu, J. Wang, X. Liu, J. Cheng, Y. Yu, Nanoscale 6 (2014) 693.
[13] J.S. Cho, J.-S. Park, Y.C. Kang, Nano Res. 10 (2017) 897.
[14] J.S. Cho, H.S. Ju, J.-K. Lee, Y.C. Kang, Nanoscale 9 (2017) 1942.
[15] B. Qu, C. Ma, G. Ji, C. Xu, J. Xu, Y.S. Meng, T. Wang, J.Y. Lee, Adv. Mater. 26 (2014) 3854.
[16] L. David, R. Bhandavat, G. Singh, ACS Nano 8 (2014) 1759.
[17] D. Chao, P. Liang, Z. Chen, L. Bai, H. Shen, X. Liu, X. Xia, Y. Zhao, S.V. Savilov, J. Lin, ACS Nano 10 (2016) 10211.
[18] G.D. Park, J.H. Kim, S.-K. Park, Y.C. Kang, ACS Appl. Mater. Interfaces 9 (2017) 10673.
[19] Y. Tang, Z. Zhao, Y. Wang, Y. Dong, Y. Liu, X. Wang, J. Qiu, ACS Appl. Mater. Interfaces 8 (2016) 32324.
[20] D. Xie, X. Xia, Y. Zhong, Y. Wang, D. Wang, X. Wang, J. Tu, Adv. Energy Mater. 7 (2017) 1601804.
[21] F. Niu, J. Yang, N. Wang, D. Zhang, W. Fan, J. Yang, Y. Qian, Adv. Funct. Mater. 27 (2017) 1700522.
[22] S.Y. Jeong, S.-K. Park, Y.C. Kang, J.S. Cho, Chem. Eng. J. 351 (2018) 559.
[23] C. Zhu, X. Mu, P.A. van Aken, Y. Yu, J. Maier, Angew. Chem. 126 (2014) 2184.
[24] Y. Lu, Q. Zhao, N. Zhang, K. Lei, F. Li, J. Chen, Adv. Funct. Mater. 26 (2016) 911.
[25] Y. Xia, B. Wang, X. Zhao, G. Wang, H. Wang, Electrochim. Acta 187 (2016) 55.
[26] Q. Liu, X. Li, Z. Xiao, Y. Zhou, H. Chen, A. Khalil, T. Xiang, J. Xu, W. Chu, X. Wu, Adv. Mater. 27 (2015) 4837.
[27] S.-K. Park, Y.C. Kang, ACS Appl. Mater. Interfaces 10 (2018) 17203.
[28] Y. Cao, L. Xiao, M.L. Sushko, W. Wang, B. Schwenzer, J. Xiao, Z. Nie, L.V. Saraf, Z. Yang, J. Liu, Nano Lett. 12 (2012) 3783.
[29] S. Vishwanath, X. Liu, S. Rouvimov, P.C. Mende, A. Azcatl, S. McDonnell, R.M. Wallace, R.M. Feenstra, J.K. Furdyna, D. Jena, 2D Mater 2 (2015) 024007.
[30] Y. Sun, X. Hu, C.Y. Jimmy, Q. Li, W. Luo, L. Yuan, W. Zhang, Y. Huang, Energy Environ. Sci. 4 (2011) 2870.
[31] J. Zhou, J. Yang, Z. Xu, T. Zhang, Z. Chen, J. Wang, J. Mater. Chem. A 5 (2017) 9350.
[32] S.-K. Park, J.K. Kim, Y.C. Kang, J. Mater. Chem. A 5 (2017) 18823.
[33] J.C. Yu, X. Hu, Q. Li, Z. Zheng, Y. Xu, Chem.-Eur. J. 12 (2006) 548.
[34] J.H. Kim, Y.C. Kang, Small 13 (2017) 1701585.
[35] R. Li, S. Wang, W. Wang, M. Cao, Phys. Chem. Chem. Phys. 17 (2015) 24803.
[36] H. Li, Y. Su, W. Sun, Y. Wang, Adv. Funct. Mater. 26 (2016) 8345.
[37] G. Shen, X. Sun, H. Zhang, Y. Liu, J. Zhang, A. Meka, L. Zhou, C. Yu, J. Mater. Chem. A 3 (2015) 24041.
[38] M. Zhuang, Y. Ding, X. Ou, Z. Luo, Nanoscale 9 (2017) 4652.
[39] Y.-Y. Chen, Y. Zhang, W.-J. Jiang, X. Zhang, Z. Dai, L.-J. Wan, J.-S. Hu, ACS Nano 10 (2016) 8851.
[40] J. Shui, F. Du, C. Xue, Q. Li, L. Dai, ACS Nano 8 (2014) 3015.
[41] Q. Li, R. Cao, J. Cho, G. Wu, Adv. Energy Mater. 4 (2014) 1301415.
[42] J.S. Cho, Y.J. Hong, Y.C. Kang, ACS Nano 9 (2015) 4026.
[43] S.Q. Chen, Y. Wang, J. Mater. Chem. 20 (2010) 9735.
[44] J.C. Groen, L.A. Peffer, J. Pérez-Ramı'rez, Microporous Mesoporous Mater. 60 (2003) 1.
[45] H. Du, L. Jiao, Q. Wang, Q. Huan, W. Peng, D. Song, Y. Wang, H. Yuan, J. Power Sources 196 (2011) 10748.
[46] S.H. Choi, Y.C. Kang, Nanoscale 7 (2015) 3965.
[47] J. Ding, H. Wang, Z. Li, A. Kohandehghan, K. Cui, Z. Xu, B. Zahiri, X. Tan, E.M. Lotfabad, B.C. Olsen, ACS Nano 7 (2013) 11004.
[48] S. Wang, L. Xia, L. Yu, L. Zhang, H. Wang, X.W. Lou, Adv. Energy Mater. 6 (2016) 1502217.
[49] J.-S. Park, S.Y. Jeong, K.M. Jeon, Y.C. Kang, J.S. Cho, Chem. Eng. J. 339 (2018) 97.
[50] B. Li, X. Li, W. Li, Y. Wang, E. Uchaker, Y. Pei, X. Cao, S. Li, B. Huang, G. Cao, ChemNanoMat 2 (2016) 281.
[51] J. Lei, W. Li, X. Li, E.J. Cairns, J. Mater. Chem. 22 (2012) 22022.
[52] H. Zhang, X. Huang, O. Noonan, L. Zhou, C. Yu, Adv. Funct. Mater. 27 (2017) 1606023.
[53] J.S. Cho, J.-S. Park, K.M. Jeon, Y.C. Kang, J. Mater. Chem. A 5 (2017) 10632.
[54] S. Kong, R. Dai, H. Li, W. Sun, Y. Wang, ACS Sustainable Chem. Eng. 3 (2015) 1830.
[55] H. Ren, R. Yu, J. Wang, Q. Jin, M. Yang, D. Mao, D. Kisailus, H. Zhao, D. Wang, Nano Lett. 14 (2014) 6679.
[56] X. Sun, H. Zhang, L. Zhou, X. Huang, C. Yu, Small 12 (2016) 3732.